Total Internal Reflection Fluorescence Correlation Spectroscopy: Effects of Lateral Diffusion and Surface-Generated Fluorescence

Jonas Ries, Eugene P. Petrov, and Petra Schwille
Biotechnologisches Zentrum, Technical University of Dresden, Dresden, Germany

ABSTRACT Fluorescence correlation spectroscopy with total internal reflection excitation (TIR-FCS) is a promising method with emerging biological applications for measuring binding dynamics of fluorescent molecules to a planar substrate as well as diffusion coefficients and concentrations at the interface. Models for correlation functions proposed so far are rather approximate for most conditions, since they neglect lateral diffusion of fluorophores. Here we propose accurate extensions of previously published models for axial correlation functions taking into account lateral diffusion through detection profiles realized in typical experiments. In addition, we consider the effects of surface-generated emission in objective-based TIR-FCS. The expressions for correlation functions presented here will facilitate quantitative and accurate measurements with TIR-FCS.

INTRODUCTION

A multitude of processes, ranging from controlled transfer of ions to immune response, are regulated at the level of the plasma membrane. The understanding of their molecular basis is among the main goals of modern biological research. Of particular interest are the concentrations and diffusion modes of membrane proteins and the interaction of membrane bound receptors with free ligands which can be studied using fluorescence correlation spectroscopy with total internal reflection excitation (TIR-FCS). Here the evanescent wave of a totally reflected laser beam is used to excite fluorophores selectively at the interface between solution and a planar substrate. The thin detection volume features an excellent surface selectivity which allows for high concentrations of fluorophores in solution and efficiently rejects a cytoplasmic background when measuring in cellular membranes. Introduced in the early 80s (1,2) it has recently been applied to study diffusion in solution (3,4), diffusion in model and cell membranes (5) and association/dissociation dynamics with membranes (6,7) or surfaces (8).

Significant theoretical work has been devoted to deriving models for TIR-FCS correlation functions which incorporate binding dynamics (2), even in presence of nonfluorescent competitors (9), and axial diffusion through the evanescent field (10). Those models are essentially one-dimensional, since they neglect the lateral diffusion through the detection volume. For free solution diffusion and pure membrane diffusion, a rather approximate lateral diffusion model has been used (4,5). As will be shown in this article, lateral diffusion significantly influences the correlation curves for most experimental conditions and has to be accurately taken into account for quantitative TIR-FCS. In objective-based TIR-FCS, surface-generated emission, collected by the high numerical aperture objective, leads to an additional confinement of the axial detection profile and affects the shape of the correlation curves.

An accurate model for TIR-FCS correlation functions is needed, since an inadequate model can lead to inexact or even completely wrong parameter estimates when applied to the analysis of experimental data, especially when complex models with several free-fitting parameters are used (i.e., combined diffusion and binding kinetics). Besides, in TIR-FCS most of the parameters determining the detection volume are accessible to the experimenter. An accurate model therefore diminishes the need of calibration measurements and eliminates additional free fit parameters describing the detection volume.

In this work, we derive an accurate extension of previously published one-dimensional axial correlation functions which allows one to take into account lateral diffusion through detection profiles realized in typical experiments. In addition, we show how to take into account surface-generated fluorescence in objective-based TIR-FCS. To get a better overview about the results presented in this article, Fig. 1 shows a summary. The correlation functions derived here should accurately describe TIR-FCS results under most experimental conditions and thus comprise the basis for accurate and quantitative interpretation of TIR-FCS measurements.

Principle of TIR-FCS

When light passes through a dielectric with a high refractive index n_2 (e.g., glass) into a dielectric with a lower refractive index n_1 (e.g., water), it is refracted toward the interface. If the incidence angle is larger than the critical angle $\theta_c = \arcsin(n_1/n_2)$, all light is reflected, and total internal reflection occurs. Although no light propagates through the interface, there is an exponentially decaying electromagnetic field above the interface, the so-called evanescent wave with the intensity profile:

Submitted November 27, 2007, and accepted for publication February 26, 2008.

Address reprint requests to Petra Schwille, Tel.: 49-351-463-40328; E-mail: schwille@biotec.tu-dresden.de.

Editor: Gerard Marriott.

0006-3495/08/07/390/10 $2.00

doi: 10.1529/biophysj.107.126193

Models and Applications of TIR-FCS

Model	Applications	Correlation Function
Free diffusion 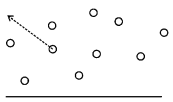	• Calibration of detection volume • FCS with small detection volume and high countrate (3, 4)	Eq. i with eq. ii or eq. 24. Objective based TIR-FCS: Eq. 35, eq. 38.
Diffusion in membrane 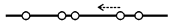	• Concentration and diffusion in membrane (5) • Rejection of cytosolic fluorescence	Eq. ii or eq. 24
Binding to surface 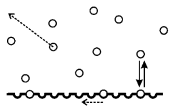	• Binding of ligand to membrane bound receptor (6, 7) • Reversible binding to surface (2) • On- and off-rates, binding constant	Eq. iii with eq. ii or eq. 24. Axial correlation functions: Eq. 50-52 and (1, 6, 9, 10).

Correlation functions for TIR-FCS

- Free diffusion of fluorophores above the surface (eq. 12 and eq. 13):

$$g(\tau) = \eta_A A g_{xy}(\tau) g_z(\tau) \tag{i}$$
$$g_z(\tau) = \sqrt{\frac{D\tau}{\pi}} - \frac{2D\tau\kappa^2 - 1}{2\kappa} w(i\sqrt{D\tau}\kappa)$$

- Lateral correlation function for square pinhole (eq. 23), good approximation for circular pinhole with effective a from Fig. 2c:

$$g_{xy}(\tau) = \frac{1}{a^2}\left(\frac{1}{\sqrt{\pi}\mu}\left(e^{-\mu^2} - 1\right) + \mathrm{erf}(\mu)\right)^2 \tag{ii}$$
$$\mu = \frac{a}{2\sqrt{\sigma^2 + D\tau}}$$

- General correlation functions for TIR-FCS which take into account binding/unbinding kinetics (eq. 26-29 and eq. 50-52):

$$\begin{aligned} g(\tau) &= \eta_A A \left(g_{AA}(\tau) + 2g_{AC}(\tau) + g_{CC}(\tau)\right) \\ g_{AA}(\tau) &= g_{AA,z}(\tau) g_{xy}(\tau; D_A) \\ g_{AC}(\tau) &= g_{AC,z}(\tau) \sqrt{g_{xy}(\tau; D_A)} \sqrt{g_{xy}(\tau; D_C)} \\ g_{CC}(\tau) &= g_{CC,z}(\tau) g_{xy}(\tau; D_C) \end{aligned} \tag{iii}$$

- In objective-based TIR-FCS the use of an effective decay length d_{eff} (Fig. 4c) can account for surface generated fluorescence.

FIGURE 1 Overview: Correlation functions for TIR-FCS discussed in this article. For details and notation, see text.

$$W(z) = \exp\left(-\frac{z}{d}\right) = \exp(-\kappa z). \tag{1}$$

The decay length $d = \frac{\lambda}{4\pi}\left(n_2^2 \sin^2\theta - n_1^2\right)^{-1/2}$ depends on the vacuum wavelength λ, the refractive indices and, most importantly, the angle of incidence θ, and can be $\ll$100 nm. Since only fluorophores in the evanescent field are excited, an excellent surface selectivity is achieved.

There are two different approaches for the practical realization of a TIR-FCS setup: a prism- and an objective-based setup (11). In the first case, a prism is used to generate high-enough incidence angles and fluorescence is collected by a microscope objective opposite to the prism (Fig. 2 *a*) (2). In the second case, the laser is focused through the periphery of a high numerical aperture objective, which is directly coupled to the surface of interest, to generate internal reflection. Emission is collected with the same objective (Fig. 2 *b*) (4). The advantages of the prism-based setup are the versatility of the optical alignment and a lower background signal, objective-based TIRF features sample-top accessibility, higher collection efficiency and commercial availability (11).

In general, the lateral extension of the TIR-excitation profile is rather large (several μm). To obtain a detection volume small enough for FCS, a pinhole in the image plane is used for lateral confinement (11). For diffusion measurements in membranes, a tight lateral confinement is especially important to obtain reasonable diffusion times (5). The drawback of this approach is significant bleaching outside the detection volume. Many fluorophores will get bleached in the large excitation spot before they can enter the detection area. Therefore, it can be a serious limitation in the study of membrane diffusion. On the other hand, TIR-FCS is well

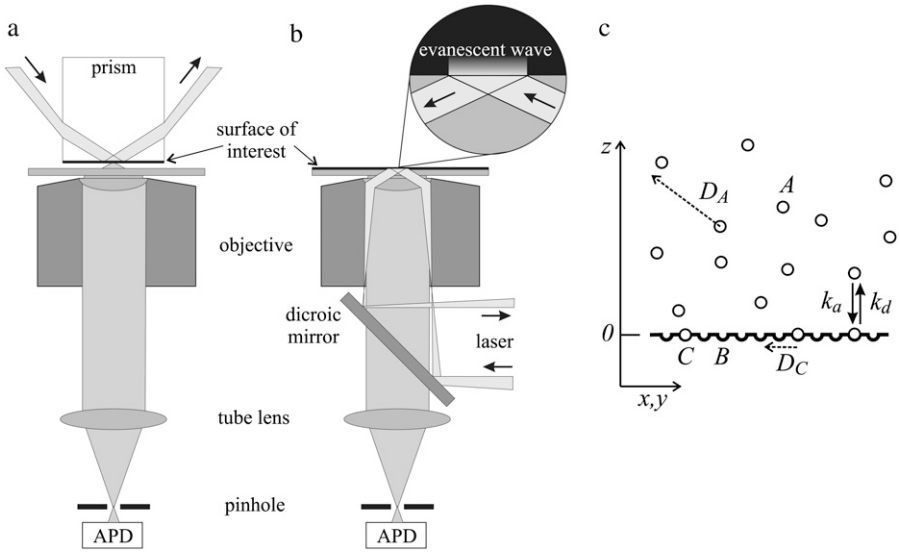

FIGURE 2 (*a*) Principle of prism-based TIR-FCS. Total internal reflection in the prism generates the evanescent field at the prism/solution interface. Emission is collected with an objective on the opposite side, spectrally filtered and detected with a single photon detector. A pinhole in the image plane is used for the lateral confinement of the detection volume. (*b*) Objective-based TIR-FCS. The laser is focused onto the periphery of the back focal plane of a high NA objective. Total internal reflection at the interface between cover slide and solution occurs. Emission is collected with the same objective. Also here a pinhole is needed for lateral confinement. (*c*) Parameters accessible with TIR-FCS: The concentration of free fluorophores *A*, of bound fluorophores *C* and of free attachment sites *B*, the association and dissociation constants k_a and k_d, the solution diffusion coefficient D_A and the diffusion coefficient for membrane-bound fluorophores D_C.

suited to study binding kinetics (6,7): Since most fluorophores are replenished via binding/unbinding rather than via membrane diffusion, out of focus photo bleaching is less of a problem.

What parameters are accessible with TIR-FCS? For free fluorophores in solution or surface-bound fluorophores, mainly the diffusion coefficient D_A or D_C and the concentration A or C, respectively, are of interest. But in general, there is an exchange between free and surface-bound fluorophores. For instance, a labeled ligand in solution can bind reversibly to a membrane-bound receptor. There are several parameters governing this situation (10) (Fig. 2 *c*): The surface association and dissociation rate constants k_a and k_d, the ligand concentration in solution A and the total receptor concentration on the membrane S and the diffusion coefficients D_A and D_C. From these parameters, additional parameters can be derived: The equilibrium constant describing surface binding $K = k_a/k_d = S/AB$, the fraction of unbound receptors $\beta = (1 + KA)$, the concentration of free receptors $B = \beta S$ and the concentration of receptor-ligand complexes $C = \beta KAS$.

Correlation functions in FCS

The normalized autocorrelation curve in FCS for a stationary system is defined as

$$G(\tau) = \frac{\langle \delta F(t)\, \delta F(t+\tau)\rangle}{\langle F(t)\rangle^2} = g(\tau)/\langle F\rangle^2, \qquad (2)$$

where $\langle f(t)\rangle = \frac{1}{T}\int_0^T f(t)dt$ denotes the time average over t with the measurement time T; $\delta F(t) = F(t) - \langle F(t)\rangle$. The nonnormalized correlation curve is $g(\tau) = \langle \delta F(t)\delta F(t+\tau)\rangle$. (Note that a widely used alternative definition of the autocorrelation curve is $\tilde{G}(\tau) = (\langle F(t)\, F(t+\tau)\rangle/\langle F(t)\rangle^2) = G(\tau)+1$, which decays to 1 instead of 0 for large lagtimes.)

The fluorescence signal for n species (e.g., free fluorophores and membrane-bound fluorophores) can be calculated from the molecule detection function $\Omega(\mathbf{r})$, the molecular brightness of each species η_i determined by quantum yields, absorption cross sections, detection efficiencies and excitation intensity, and the time- and position-dependent concentrations $C_i(\mathbf{r}, t)$:

$$F(t) = \sum_{i=1}^{n} \int d^3\mathbf{r}\, \eta_i \Omega(\mathbf{r}) C_i(\mathbf{r}, t). \qquad (3)$$

Equation 2 can be evaluated with Eq. 3 to calculate the nonnormalized correlation function,

$$g(\tau) = \sum_{i=1}^{n}\sum_{j=1}^{n} g_{ij}(\tau), \qquad (4)$$

with

$$g_{ij}(\tau) = \eta_i \eta_k \int\int d^3\mathbf{r} d^3\mathbf{r}'\, \Omega(\mathbf{r}) \phi_{ij}(\mathbf{r}, \mathbf{r}', \tau) \Omega(\mathbf{r}') \qquad (5)$$

and the concentration correlation functions

$$\phi_{ij}(\mathbf{r}, \mathbf{r}', \tau) = \langle \delta C_i(\mathbf{r}, 0)\, \delta C_j(\mathbf{r}', \tau)\rangle. \qquad (6)$$

To further calculate the correlation functions, $\Omega(\mathbf{r})$ and the ϕ_{ij} have to be specified.

Axial correlation functions for TIR-FCS

Considerable work has been devoted to finding TIR-correlation functions taking into account solution diffusion, binding dynamics (10), and the presence of nonfluorescent competitors (9), albeit only considering the motion along the axial dimension (z axis in Fig. 2). These correlation functions we call axial correlation functions. Here we use the framework and notation presented in Starr and Thompson (10) to develop extensions to incorporate lateral diffusion and surface-generated fluorescence. More refined one-dimensional TIR-models can be extended in the same way to include lateral diffusion and surface-generated fluorescence.

The axial correlation function in TIR-FCS describing binding dynamics has contributions from free fluorophores in solution, surface-bound fluorophores, and from the cross-correlation between free and surface-bound fluorophores (10):

$$g_z(\tau) = g_{AA,z}(\tau) + 2g_{AC,z}(\tau) + g_{CC,z}(\tau). \quad (7)$$

The rather lengthy expressions for $g_{AA,z}(\tau)$, $g_{AC,z}(\tau)$, and $g_{CC,z}(\tau)$ as well as details about the derivation are given in the Appendix.

Three-dimensional correlation functions for TIR-FCS

The axial correlation functions for TIR-FCS derived in the literature (9,10) and Eq. 7 take into account in detail the binding dynamics but neglect lateral diffusion. As will be shown later, lateral diffusion significantly influences the correlation curves for virtually all experimental conditions. In the following sections we will show how to incorporate lateral diffusion in TIR-FCS. We discuss the case of free diffusion for which an analytical solution exists, derive lateral correlation functions for several lateral detection profiles relevant for TIR-FCS and finally present semiempirical, but quite accurate three-dimensional correlation functions for TIR-FCS which include binding dynamics. A nonplanar membrane topology and/or undulatory dynamics, which can lead to additional difficulties in the interpretation of FCS correlation curves, are not discussed in this work.

Diffusion without binding

For three-dimensional diffusion in solution in the upper half-space ($z > 0$) bounded at $z = 0$ by a reflective boundary with the diffusion coefficient D and the mean concentration A, the concentration correlation function factorizes into its axial and lateral part. Here we neglect a dependence of the diffusion coefficients on the distance to the surface (12,13), which is only important for relatively large fluorescent particles (14). The concentration correlation function for free diffusion is

$$\phi_{AA}(\mathbf{r}, \mathbf{r}', z, z', \tau) = \eta_A A \phi_{AA,xy}(\mathbf{r}, \mathbf{r}', \tau)\, \phi_{AA,z}(z, z', \tau), \quad (8)$$

$$\phi_{AA,xy}(\mathbf{r}, \mathbf{r}', \tau) = \frac{1}{4D\pi\tau} \exp\left(-\frac{(\mathbf{r} - \mathbf{r}')^2}{4D\tau}\right), \quad (9)$$

$$\phi_{AA,z}(z, z', \tau) = \frac{1}{\sqrt{4D\pi\tau}} \left(\exp\left(-\frac{(z - z')^2}{4D\tau}\right) + \exp\left(-\frac{(z + z')^2}{4D\tau}\right)\right). \quad (10)$$

For TIR-FCS the molecule detection function $\Omega(x, y, z)$ can be written as the product of the lateral detection profile $L(x, y)$ and the axial profile $W(z)$:

$$\Omega(x, y, z) = L(x, y)W(z). \quad (11)$$

Since both the concentration correlation function and the molecule detection function factorize into a lateral and an axial part, so do the correlation functions:

$$g(\tau) = \eta_A A g_{xy}(\tau) g_z(\tau). \quad (12)$$

For the exponential TIR-excitation profile $W(z) = \exp(-\kappa z)$ the axial correlation function is the well-known TIR-FCS correlation function which can be calculated with Eq. 10 in Eq. 5,

$$g_z(\tau) = \sqrt{\frac{D\tau}{\pi}} - \frac{2D\tau\kappa^2 - 1}{2\kappa} w(i\sqrt{D\tau}\kappa), \quad (13)$$

with

$$w(i\xi) = e^{\xi^2} \operatorname{erfc}(\xi). \quad (14)$$

The lateral correlation function $g_{xy}(\tau)$ depends on the shape of lateral detection profile $L(x, y)$. Several profiles relevant for TIR-FCS (Fig. 3 *a*) will be discussed in the following section.

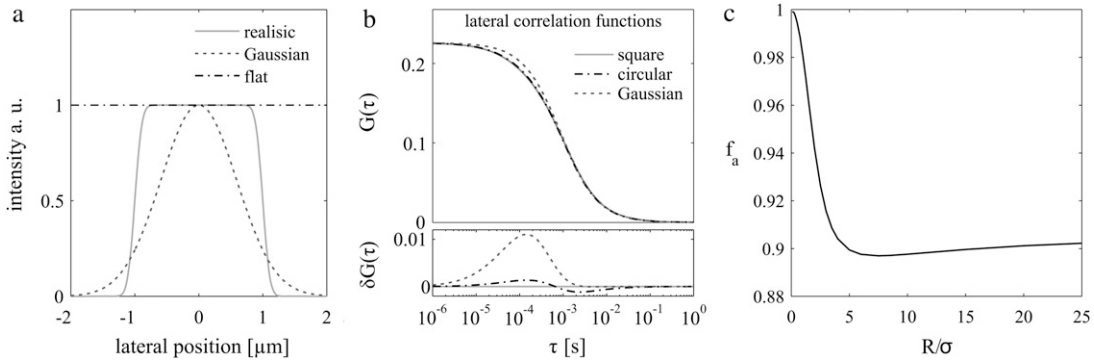

FIGURE 3 (*a*) Typical lateral profiles. Square pinhole of size $a = 2\ \mu$m, numerical aperture of the objective: NA = 1.2 (—). Gaussian approximation with a waist of $w_0 = 1.19\ \mu$m which results in the same effective detection area (– – –). Flat profile neglecting lateral diffusion (– · –). (*b*) Lateral correlation functions for a square pinhole with $a = 2\ \mu$m (—), a circular pinhole with $R = 1.11\ \mu$m (– · –), and a Gaussian profile with $w_0 = 1.19\ \mu$m (– – –). (*c*) Approximation of a circular pinhole (radius R) with a square pinhole with $a = 2Rf_a$. f_a was obtained by numerically calculating correlation curves for a circular pinhole and fitting them with the correlation functions for a square pinhole (Eq. 22).

Lateral detection profiles

If lateral diffusion is neglected, $g_{xy} = A_{eff}$ is a constant factor taking into account the size of the detection area. This approach has been used in the literature (6,7,9–11).

A common approximation of the lateral detection profile is a two-dimensional Gaussian (4,5):

$$L(x,y) = \frac{2}{\pi w_0^2}\exp\left(-2\frac{x^2+y^2}{w_0^2}\right). \tag{15}$$

In this case,

$$g_{xy}(\tau) = \frac{1}{\pi w_0^2}\left(1+\frac{4D\tau}{w_0^2}\right)^{-1}. \tag{16}$$

For TIR-FCS this approach is only satisfactory for pinholes much smaller than the Airy disk, but this case is accompanied by a loss in molecular brightness. Also the effective axial extension w_0 is an empirical parameter and has to be determined with a calibration measurement. This is unfortunate, since in TIR-FCS the parameters describing the lateral detection profile (pinhole size and shape and numerical aperture of the objective) are usually well known. Here we propose a more accurate model, valid for a laterally homogeneous excitation profile and arbitrary pinhole sizes.

The detection profile is given by the image of the pinhole in the sample space, convoluted with the point-spread function of the objective, which can be approximated by a Gaussian of width $\sigma = 0.21\lambda/\mathrm{NA}$ (15):

$$\mathrm{PSF}(x-x_0) = \frac{1}{\sqrt{2\pi}\sigma}\exp\left(-\frac{(x-x_0)^2}{2\sigma^2}\right). \tag{17}$$

Here we consider two different pinhole types—square-shaped and circular ones. In charge-coupled-device-based TIR-FCS the pixels of the camera work essentially as square pinholes. But also pinholes of variable size are usually rectangular. For a square pinhole of size a in the object plane, the detection profile $L_{xy}(x,y) = L_x(x)L_x(y)$ is described by (Fig. 3 *a*):

$$\begin{aligned} L_x(x) &= \frac{1}{a}\int_0^a \mathrm{PSF}(x-x_0)dx_0 \\ &= \frac{1}{2a}\left(\mathrm{erf}\left(\frac{(a-x)}{\sqrt{2}\sigma}\right)+\mathrm{erf}\left(\frac{x}{\sqrt{2}\sigma}\right)\right). \end{aligned} \tag{18}$$

For a circular pinhole of radius R the radial profile is given by

$$\begin{aligned} L_r(r) &= \frac{1}{4R}\left(\mathrm{erf}\left(\frac{(R-r)}{\sqrt{2}\sigma}\right)+\mathrm{erf}\left(\frac{R+r}{\sqrt{2}\sigma}\right)\right) \\ r^2 &= x^2+y^2. \end{aligned} \tag{19}$$

Lateral correlation functions

For the square pinhole, the correlation function can readily be calculated, since the profile, as well as the concentration correlation function, factorize as

$$\phi_{AA,xy}(\mathbf{r},\mathbf{r}',\tau) = \phi_{AA,x}(x,x',\tau)\phi_{AA,x}(y,y',\tau), \tag{20}$$

$$\phi_{AA,x}(x,x',\tau) = \frac{1}{\sqrt{4D\pi\tau}}\exp\left(-\frac{(x-x')^2}{4D\tau}\right), \tag{21}$$

then

$$g_{xy}(\tau) = g_x(\tau)^2 \tag{22}$$

and

$$\begin{aligned} g_x(\tau) &= \int_{-\infty}^{\infty}dx\int_{-\infty}^{\infty}dx' L_x(x)\phi_{AA,x}(x,x',\tau)L_x(x') \\ &= \frac{1}{a^2}\int_0^a dx_0\int_0^a dx_0'\int_{-\infty}^{\infty}dx\int_{-\infty}^{\infty}dx'\mathrm{PSF}(x-x_0)\phi_{AA,x}(x,x',\tau)\mathrm{PSF}(x'-x_0') \\ &= \frac{2}{a^2\sqrt{\pi}}\sqrt{\sigma^2+D\tau}\left(\exp\left(-\frac{a^2}{4(\sigma^2+D\tau)}\right)-1\right)+\frac{1}{a}\mathrm{erf}\left(\frac{a}{2\sqrt{\sigma^2+D\tau}}\right). \end{aligned} \tag{23}$$

Since the molecule detection function for the circular pinhole (Eq. 19) does not factorize in the x and y part, an analytical solution could not be found. The correlation functions have to be calculated numerically. Here we propose a fast numerical implementation, based on the Fourier transformation (16). The correlation function can be written in terms of the Fourier transforms of the profile $\tilde{L}(k_x,k_y)$ and the concentration correlation function $\tilde{\phi}_{AA,xy}(k_x,k_y,\tau)$:

$$\begin{aligned} g_{xy}(\tau) &= \int\int dxdy\int\int dx'dy' L(x,y)\phi_{AA,xy}(x-x',y-y',\tau) \\ &\quad\times L(x',y') \\ &= \int\int dk_x dk_y |\tilde{L}(k_x,k_y)|^2\tilde{\phi}_{AA,xy}(k_x,k_y,\tau). \end{aligned} \tag{24}$$

The value $\tilde{\phi}_{AA,xy}$ can be evaluated directly with Eq. 9:

$$\tilde{\phi}_{AA,xy}(k_x,k_y,\tau) = e^{-D\tau(k_x^2+k_y^2)}. \tag{25}$$

The expression $\tilde{L}(k_x,k_y)$ can be calculated numerically from $L(x,y)$, for example by using the Fast Fourier transform. The maximal x and y, as well as the grid size, should be chosen with care to minimize computation times and maximize the accuracy.

Another approach is to approximate the circular profile with an effective square profile and to fit the curves with Eq. 23 (Fig. 3 *b*). This works reasonably well if an effective $a = 2Rf_a(R/\sigma)$ is used. The correction factor f_a depends on the ratio between the pinhole radius R in the object plane and width σ of the point-spread function and its dependence is shown in Fig. 3 *c*. The resulting error in the diffusion coefficient is $<0.2\%$ for any pinhole size, the error in the concentration is $<5\%$. However, the shapes of correlation functions for a square pinhole and a corresponding circular pinhole are not the same (Fig. 3 *b*). This deviation can lead to wrong parameter estimates if additional fit parameters are used; for instance, if binding kinetics are considered.

3D-TIR-FCS

When surface binding/unbinding is present, the concentration correlation functions do not factorize any more into a lateral and an axial part. Even an analytical solution for the corresponding differential equations could only be found in the one-dimensional limit neglecting lateral diffusion. But those one-dimensional correlation functions differ enormously from the correct three-dimensional ones, as can be seen in Fig. 4 from the comparison with a simulated curve. We found that for virtually all experimental conditions the lateral diffusion cannot be neglected. Even for lateral dimensions a exceeding the axial decay length d 100-fold, the fitting of a three-dimensional correlation curve with the one-dimensional model results in an error of 15% in the diffusion coefficient D in the case of free diffusion. For more typical conditions, when $a = 10d$ ($a = 20d$, $a = 30d$), the error in D is 150% (70%, 50%). If binding kinetics are considered, the additional fit parameters, combined with the difference in shape between one- and three-dimensional correlation functions, will lead to even higher errors. The reason for this strong effect is the fact that the one-dimensional correlation functions fall off only extremely slowly with large lag times. Lateral diffusion provides an additional route for the particles to escape and thus depresses this long tail.

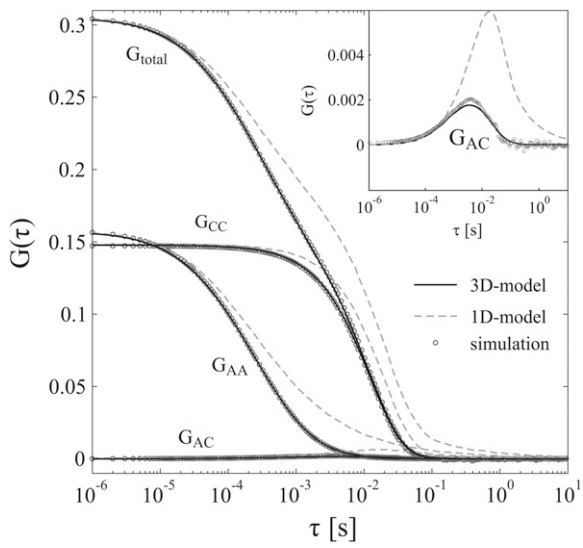

FIGURE 4 Simulated correlation curve (○), three-dimensional correlation function including lateral diffusion (—) and axial correlation function (– – –). For details, see Appendix. Parameters: $D_A = 50\ \mu m^2/s$, $D_C = 2\ \mu m^2/s$, $k_a = 5 \times 10^6\ M^{-1}\ s^{-1}$, $k_d = 50\ s^{-1}$, $A = 50$ nM, $S = 200\ \mu m^{-2}$, and $d = 0.07\ \mu m$, square pinhole with $a = 0.7\ \mu m$ and $\sigma = 0.1\ \mu m$. Box for Simulation: $10 \times 10 \times 5\ \mu m^3$. 10^9 steps of 1 μs. (*Inset*) Magnification of $G_{AC}(\tau)$.

Here we propose a semiempirical, but accurate extension of the axial correlation functions to three dimensions to include lateral diffusion. The extensions are based on the solution for free diffusion (Eq. 12) and verified by simulations. As in the one-dimensional case (Eq. 7), the correlation function for binding has contributions from free fluorophores in solution, surface-bound fluorophores, and from the cross-correlation between free and surface-bound fluorophores:

$$g_{AA}(\tau) = g_{AA,z}(\tau)g_{xy}(\tau; D_A), \tag{26}$$

$$g_{AC}(\tau) = g_{AC,z}(\tau)\sqrt{g_{xy}(\tau; D_A)}\sqrt{g_{xy}(\tau; D_C)}, \tag{27}$$

$$g_{CC}(\tau) = g_{CC,z}(\tau)g_{xy}(\tau; D_C), \tag{28}$$

$$g(\tau) = \eta_A A(g_{AA}(\tau) + 2g_{AC}(\tau) + g_{CC}(\tau)). \tag{29}$$

D_A and D_C are the diffusion coefficients for free fluorophores in solution and surface-bound fluorophores, respectively, and $g_{xy}(\tau;D)$ denotes that the diffusion coefficient D is used in the corresponding lateral correlation function. Note that the axial correlation functions still depend on the concentrations A and C as well as the molecular brightnesses η_A and η_C (Eqs. 50–52). The semiempirical extension presented here approaches the analytical solution (Eq. 12) in the limit of free diffusion and perfectly matches the simulated correlation curves within the accuracy of the simulation (Fig. 4).

To calculate the normalized correlation function $G(\tau)$, the total average intensity has to be evaluated with Eq. 3. Then

$$G(\tau) = \frac{g(\tau)}{\langle F_{tot}\rangle^2}, \tag{30}$$

$$\langle F_{tot}\rangle = F_A + F_C = \left(\int dxdyL(x,y)\right) \times \left(\eta_A A \int dzW(z) + \eta_C CW(0)\right). \tag{31}$$

Note that η_A and η_C can be different: First, surface-bound fluorophores can have a preferred orientation. This leads to photoselection in the excitation and a change in the emission profile. Second, the micro environment can influence the quantum yields and spectra and therefore the molecular brightness of surface-bound fluorophores.

Supercritical detection in objective-based TIR-FCS

Fluorophores close to a water-glass interface can couple their emission directly into the glass. This surface-generated fluorescence is emitted into supercritical angles. In objective-

based TIR-FCS high-NA objectives are used which collect a significant portion of the supercritical fluorescence. This leads to a further axial confinement of the detection volume.

Axial profile

For objective-based TIR-FCS the axial profile $W(z) = S(z)\exp(-\kappa z)$ of the molecule detection function is a product of the exponential excitation profile with the collection efficiency function $S(z)$, which takes into account surface-generated fluorescence. Surface-generated fluorescence emitted into supercritical angles leads to a stronger multiexponential confinement. It is useful to consider under- and supercritical detection separately:

$$W(z) = W_u(z) + W_s(z). \tag{32}$$

Expressions for $W_u(z)$ and $W_s(z)$ are derived in the Appendix for randomly oriented molecules. For the case of oriented molecules, see Ries et al. (17). We find for the undercritical part:

$$W_u(z) = e^{-kz}\int_{w_a}^{w_b} f_u(w_1)dw_1$$
$$f_u(w_1) = \frac{cp^2 w_1 w_2}{3\lambda^3}\left(\frac{1}{(w_1+w_2)^2} + \frac{n_1^2 n_2^2}{\left(n_1^2 w_2 + n_2^2 w_1\right)^2}\right). \tag{33}$$

Here, $w_2 = \sqrt{\lambda^2 w_1^2 - n_1^2 + n_2^2}/\lambda$, $w_a = 0$, $w_b = n_1/\lambda$ and $\lambda = \lambda/2\pi$.

The supercritical axial detection profile is

$$W_s(z) = \int_{\tilde{w}_a}^{\tilde{w}_b} d\tilde{w}_1 f_s(\tilde{w}_1) e^{-(\kappa + 2\tilde{w}_1)z}$$
$$f_s(\tilde{w}_1) = \frac{cp^2\left(n_1^2+n_2^2\right)\tilde{w}_1\tilde{w}_2\left(n_2^2\tilde{w}_1^2 + n_1^2\tilde{w}_2^2\right)}{3\lambda^3\left(\tilde{w}_1^2+\tilde{w}_2^2\right)\left(\tilde{w}_2^2 n_1^4 + n_2^4\tilde{w}_1^2\right)}. \tag{34}$$

Here, $\tilde{w}_2 = \sqrt{n_2^2 - n_1^2 - \lambda^2\tilde{w}_1^2}/\lambda$, $\tilde{w}_a = 0$, and $\tilde{w}_b = \sqrt{NA^2 - n_1^2}/\lambda$.

Axial detection profiles with and without supercritical detection are shown in Fig. 5 *a*. As can be seen, surface enhanced fluorescence leads to a faster decay of the axial profile. The detection profile derived in this section can be used to calculate axial correlation functions for TIR-FCS taking into account surface-generated emission.

Correlation function

Here we derive only the axial correlation function; lateral diffusion can be included as described above. As before, we consider the contributions from the fluorophores in solution, the membrane-bound fluorophores and the cross-correlation term separately. For the free fluorophores we find

$$\begin{aligned} g_{AA,z}(\tau) &= \int_0^\infty dz \int_0^\infty dz' W(z)\phi_{AA,z}(z,z',\tau)W(z') \\ &= \int_0^\infty dz \int_0^\infty dz' W_u(z)\phi_{AA,z}(z,z',\tau)W_u(z') \\ &\quad + 2\int_0^\infty dz \int_0^\infty dz' W_u(z)\phi_{AA,z}(z,z',\tau)W_s(z') \\ &\quad + \int_0^\infty dz \int_0^\infty dz' W_s(z)\phi_{AA,z}(z,z',\tau)W_s(z') \\ &= g_{AA,z}^{uu} + 2g_{AA,z}^{us} + g_{AA,z}^{ss}, \end{aligned} \tag{35}$$

$$\begin{aligned} g_{AA,z}^{uu} &= \left(\int_{w_a}^{w_b} f_u(w_1)dw_1\right)^2 \tilde{g}_{AA}(\tau,\kappa,\kappa) \\ g_{AA,z}^{us} &= \left(\int_{w_a}^{w_b} f_u(w_1)dw_1\right)\int_{\tilde{w}_a}^{\tilde{w}_b} d\tilde{w}_1 f_s(\tilde{w}_1)\tilde{g}_{AA}(\tau,\kappa,\kappa+2\tilde{w}_1) \\ g_{AA,z}^{ss} &= \int_{\tilde{w}_a}^{\tilde{w}_b} d\tilde{w}_1 \int_{\tilde{w}_a}^{\tilde{w}_b} d\tilde{w}_1' f_s(\tilde{w}_1) f_s(\tilde{w}_1')\tilde{g}_{AA}(\tau,\kappa+2\tilde{w}_1,\kappa+2\tilde{w}_1'). \end{aligned} \tag{36}$$

The expression $\tilde{g}_{AA}(\tau,\kappa,\kappa')$ is the TIR-correlation function generalized for different decay parameters $\kappa \neq \kappa'$ and defined as

$$\tilde{g}_{AA}(\tau,\kappa,\kappa') = \int_0^\infty dz \int_0^\infty dz' e^{-\kappa z}\phi_{AA,z}(z,z',\tau)e^{-\kappa' z'}. \tag{37}$$

For concentration correlation functions which lead to analytical correlation functions for the usual TIR-profile ($\kappa = \kappa'$), usually also analytical solutions for $\tilde{g}_{AA}(\tau,\kappa,\kappa')$ can be found. The further integration over w_1 and $\tilde{w}_1$, respectively, can usually not be performed in a closed form, but the integrals are well behaved and can be solved efficiently numerically. In case of pure diffusion

$$\tilde{g}_{AA}(\tau,\kappa,\kappa') = \frac{\kappa\, w(i\sqrt{D\tau}\kappa') - \kappa'\, w(i\sqrt{D\tau}\kappa)}{\kappa^2 - \kappa'^2}. \tag{38}$$

For the cross-correlation term between surface-bound and free fluorophores we find

$$\begin{aligned} g_{AC,z}(\tau) &= \int_0^\infty dz(W_u(z) + W_s(z))\phi_{AC,z}(z,\tau) \\ &= \int_{\tilde{w}_a}^{\tilde{w}_b} d\tilde{w}_1 f_s(\tilde{w}_1)\tilde{g}_{AC}(\tau,\kappa+2\tilde{w}_1) \\ &\quad + \left(\int_{w_a}^{w_b} dw f_u(w)\right)\tilde{g}_{AC}(\tau,\kappa) \end{aligned} \tag{39}$$

with the usual TIR correlation function

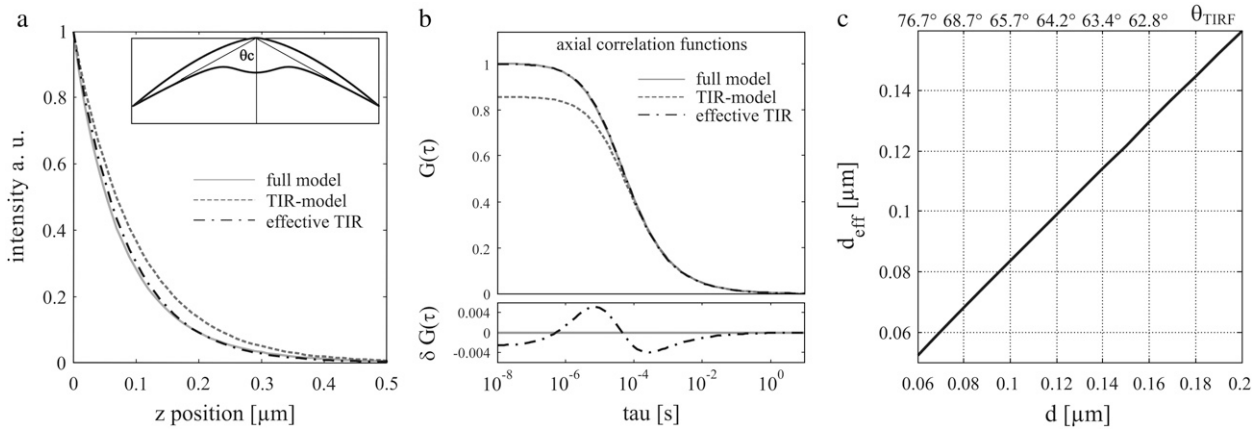

FIGURE 5 (*a*) Axial detection profiles for TIR-FCS including surface-generated fluorescence (—), exponential TIR-model (– – –) and exponential TIR-model with an effective decay length d_{eff} from Eq. 44 (– · –). (*Inset*) Polar plot of the emission profile for a fluorophore at $z = 0$. (*b*) Axial correlation functions. $\delta G(\tau)$ describes the deviation of the effective TIR-model from the full model. (*c*) Effective decay length d_{eff} to use the exponential axial model. Parameters: NA = 1.45, $d = 0.1$ μm, $D = 400$ μm^2/s, and $\lambda = 0.488$ μm.

$$\tilde{g}_{\text{AC}}(\boldsymbol{\tau}, \boldsymbol{\kappa}) = \int_0^\infty dz e^{-\kappa z} \phi_{\text{AC,z}}(z, \boldsymbol{\tau}). \tag{40}$$

The membrane term is hardly affected, only the enhanced brightness has to be taken into account,

$$g_{\text{CC,z}}(\boldsymbol{\tau}) = W(0)\phi_{\text{CC,z}}(\boldsymbol{\tau}), \tag{41}$$

with

$$W(0) = W_{\text{u}}(0) + W_{\text{s}}(0) = \int_{w_a}^{w_b} f_{\text{u}}(w_1)dw_1 + \int_{\tilde{w}_a}^{\tilde{w}_b} f_{\text{s}}(\tilde{w}_1)d\tilde{w}_1. \tag{42}$$

The mean intensity needed for normalization is (compare Eqs. 31, 42, 57, and 61):

$$\langle F_{\text{tot}} \rangle = \left(\int dxdyL(x, y) \right) (\eta_{\text{A}} A(F_{\text{s}} + F_{\text{u}}) + \eta_{\text{C}} CW(0)). \tag{43}$$

As can be seen in Fig. 5 *b*, the additional confinement of surface-generated fluorescence leads to an enlarged amplitude and faster decay of the correlation function. However, the correlation curve calculated with the full model can be well approximated with the simple TIR-model, if an effective decay length d_{eff} is chosen. For the parameters used in Fig. 5, we find an almost linear relationship between the TIR-decay length d and the effective decay length d_{eff} (Fig. 5 *c*) with

$$d_{\text{eff}} = 0.767d + 0.0068\,\mu\text{m}. \tag{44}$$

Only for large d and if special accuracy is needed, the full model should be applied.

CONCLUSION

Models for correlation functions used so far in TIR-FCS usually neglect lateral diffusion or include it in a rather approximate way. We investigated the effect of lateral diffusion in TIR-FCS and found that it significantly influences the correlation functions even for pinhole sizes in the object plane much larger than the axial decay length. This seems surprising at first, but can be fully explained by the slow decay of correlation functions describing one-dimensional diffusion. Therefore, for virtually any experimental condition, lateral diffusion should be taken into account. This can be done with the refined correlation functions presented here. They are exact if binding dynamics can be neglected. In the presence of binding/unbinding dynamics, they are still very accurate, as is demonstrated by a comparison with a simulated correlation curve. We propose lateral correlation functions valid for a square or a circular pinhole of any size which should be used in TIR-FCS instead of the approximate Gaussian model.

In objective-based TIR-FCS, the presence of surface-generated fluorescence leads to a further axial confinement of the detection volume. We present an exact model taking this effect into account and show that for most experimental conditions, the much simpler TIR-model, albeit with an effective decay length, can be used.

In our approach, the correlation functions are described fully by well-determined parameters determining the geometry of the detection volume, and no empirical parameters have to be added. This has the advantage that no calibration measurements are required. In the case where the exact TIR-angle is not known, it can be determined accurately by a calibration measurement.

In conclusion, the correlation functions presented in this work are accurate for most experimental conditions and will enable quantitative and accurate measurements with TIR-FCS.

APPENDIX

Axial correlation functions for TIR-FCS

The concentration correlation functions presented here describing binding dynamics and axial diffusion are taken from Starr and Thompson (10)

$$\phi_{CC,z}(\tau) = \frac{\eta_C C}{\eta_A A}\frac{\beta}{R_1^{1/2} - R_2^{1/2}}\Big\{R_1^{1/2} w\Big[-i(R_2\tau)^{1/2}\Big] - R_2^{1/2} w\Big[-i(R_1\tau)^{1/2}\Big]\Big\}, \quad (45)$$

$$\phi_{AC,z}(z,\tau) = \phi_{CA,z}(z,\tau) = \frac{\eta_C C}{\eta_A A}\frac{k_d}{D^{1/2}\left(R_1^{1/2} - R_2^{1/2}\right)} e^{-z^2/4D\tau} \times \left\{ w\left[\frac{iz}{(4D\tau)^{1/2}} - i(R_1\tau)^{1/2}\right] - w\left[\frac{iz}{(4D\tau)^{1/2}} - i(R_2\tau)^{1/2}\right]\right\}. \quad (46)$$

$$\phi_{AA,z}(z,z',\tau) = \frac{1}{(4\pi D\tau)^{1/2}}\left(e^{-\frac{(z-z')^2}{4D\tau}} + e^{-\frac{(z+z')^2}{4D\tau}}\right) - \frac{\eta_C C}{\eta_A A}\frac{k_d}{D\left(R_1^{1/2} - R_2^{1/2}\right)} e^{-\frac{(z+z')^2}{4D\tau}} \times \left\{ R_1^{1/2} w\left[\frac{i(z+z')}{(4D\tau)^{1/2}} - i(R_1\tau)^{1/2}\right] - R_2^{1/2} w\left[\frac{i(z+z')}{(4D\tau)^{1/2}} - i(R_2\tau)^{1/2}\right]\right\}. \quad (47)$$

Here

$$R_{3,4}^{1/2} = R_{1,2}^{1/2} + R_e^{1/2}$$
$$R_{1,2}^{1/2} = -\frac{R_r}{2R_t^{1/2}} \pm \left(\frac{R_r^2}{4R_t} - R_r\right)^{1/2}, \quad (48)$$

with

$$R_r = k_a A + k_d, \quad R_t = D\left(\frac{A}{\beta C}\right)^2, \quad R_e = \frac{D}{d^2}. \quad (49)$$

The corresponding nonnormalized correlation functions can be calculated with Eq. 5 and an exponential profile $W(z) = \exp(-z/d)$. For details see (10):

$$g_{CC,z}(\tau) = \frac{\eta_C C}{\eta_A A}\frac{\beta\left(R_1^{1/2} w\left[-i(\tau R_2)^{1/2}\right] - R_2^{1/2} w\left[-i(\tau R_1)^{1/2}\right]\right)}{R_1^{1/2} - R_2^{1/2}}, \quad (50)$$

Axial profile for objective-based TIR-FCS

The axial profile $W(z) = S(z)\exp(-\kappa z)$ of the molecule detection function in TIR is a product of the exponential excitation profile with the collection efficiency function $S(z)$ which takes into account supercritical emission. Surface-generated fluorescence into supercritical angles leads to a further multiexponential confinement, whereas for undercritical angles there is no further axial confinement. Therefore it is useful to consider under- and supercritical detection separately: $S(z) = S_u + S_s(z)$. Note that the undercritical part S_u is independent of z.

The derivation of $S(z)$ follows Enderlein et al. (18). There the Weyl representation of an oscillating dipole is used to calculate its emission profile close to a dielectric surface. The wave vector of the incident light is $\boldsymbol{k_1} = (\mathbf{q} \pm w_1)$. Equation 20 in Enderlein et al. (18), which describes the emission profile of a fluorophore at a distance z_0 from the interface, can then be written for undercritical angles as

$$d^2 S_u = \frac{c w_2^2}{8\pi w_1^2 \lambda\!\!\!^{-4}}\left(|T_p \hat{\boldsymbol{k}}_{p1}\cdot\mathbf{p}|^2 + |T_s \hat{\boldsymbol{k}}_s\cdot\mathbf{p}|^2\right) d\Omega^2, \quad (53)$$

where c is the speed of light, $\lambda\!\!\!^{-} = \lambda/2\pi$ the reduced wavelength, n_1 and n_2 are the refractive indices above and below the phase boundary, $w_2 = (n_2^2/\lambda\!\!\!^{-2} - q^2)^{1/2} = (\lambda\!\!\!^{-2} w_1^2 - n_1^2 + n_2^2)^{1/2}/\lambda\!\!\!^{-}$, and $\hat{\mathbf{k}}_{p1}$ and $\hat{\mathbf{k}}_s$ are unit vectors defined in Enderlein et al. (18). T_p and T_s are the transmission coefficients for plane p and s waves:

$$T_p = \frac{2 n_1 n_2 w_1}{w_1\epsilon_2 + w_2\epsilon_1}, \quad T_s = \frac{2 w_1}{w_1 + w_2}. \quad (54)$$

Here we consider the case of randomly oriented molecules in solution. In this case, $\langle|\hat{\kappa}_{p1}\cdot\mathbf{p}|^2\rangle = \langle|\hat{\kappa}_s\cdot\mathbf{p}|^2\rangle = p^2/3$ and the emission profile becomes rotationally symmetric. Using $d\Omega^2 = \frac{\lambda d^2\mathbf{q}}{n_2 w_2}$ (Eq. 22 in (18)) the integration over the detection angle can be substituted by an integration over q and one integration can be carried out: $d^2\mathbf{q} = 2\pi q dq = 2\pi q\frac{dq}{dw_1}dw_1 = -2\pi w_1 dw_1$ since $q = (n_1^2/\lambda\!\!\!^{-2} - w_1^2)^{1/2}$. Then

$$g_{AC,z}(\tau) = \frac{\eta_C C k_d}{\eta_A A}\frac{R_4^{1/2} w\left[-i(\tau R_1)^{1/2}\right] - R_3^{1/2} w\left[-i(\tau R_2)^{1/2}\right] + \left(R_1^{1/2} - R_2^{1/2}\right) w\left[i(\tau R_e)^{1/2}\right]}{\left(R_1^{1/2} - R_2^{1/2}\right)(R_3 R_4)^{1/2}}, \quad (51)$$

$$g_{AA,z}(\tau) = d\left(\frac{\tau R_e}{\pi}\right)^{1/2} - \frac{1}{2} d(2\tau R_e - 1) w\left[i(\tau R_e)^{1/2}\right] - \frac{\eta_C C}{\eta_A A}\frac{k_d}{\left(R_1^{1/2} - R_2^{1/2}\right)} \times \left\{\frac{R_1^{1/2}}{R_3}\left(w\left[-i(\tau R_1)^{1/2}\right] + (2\tau(R_1 R_e)^{1/2} + 2\tau R_e - 1) w\left[i(\tau R_e)^{1/2}\right] - 2\left(\frac{\tau R_3}{\pi}\right)^{1/2}\right) - \frac{R_2^{1/2}}{R_4}\left(w\left[-i/(\tau R_2)^{1/2}\right] + (2\tau(R_2 R_e)^{1/2} + 2\tau R_e - 1) w\left[i(\tau R_e)^{1/2}\right] - 2\left(\frac{\tau R_4}{\pi}\right)^{1/2}\right)\right\}. \quad (52)$$

$$S_u = \int_{w_a}^{w_b} f_u(w_1)dw_1, \tag{55}$$

$$f_u(w_1) = \frac{cp^2 w_1 w_2}{3\lambda^3}\left(\frac{1}{(w_1+w_2)^2} + \frac{n_1^2 n_2^2}{\left(n_1^2 w_2 + n_2^2 w_1\right)^2}\right), \tag{56}$$
$$w_a = 0 \quad \text{and} \quad w_b = n_1/\lambda.$$

The integrated undercritical axial profile is

$$F_u = \int_0^\infty dz W_u(z) = \frac{1}{\kappa}\int_{w_a}^{w_b} dw_1 f_u(w_1). \tag{57}$$

For supercritical emission w_1 in Eq. 20 in Enderlein et al. (18) is imaginary, so here it is substituted by the real and positive $\tilde{w}_1$: $w_1 = i\tilde{w}_1$:

$$d^2S_s = \frac{cw_2^2}{8\pi\tilde{w}_1^2\lambda^4}\left(|T_p\hat{\kappa}_{p1}\cdot\mathbf{p}|^2 + |T_s\hat{\kappa}_s\cdot\mathbf{p}|^2\right)\exp(-2\tilde{w}_1 z_0)d\Omega^2. \tag{58}$$

Now

$$|T_p|^2 = \frac{4n_1^2 n_2^2 \tilde{w}_1^2}{w_2^2 n_1^4 + \tilde{w}_1^2 n_2^4}, \quad |T_s|^2 = \frac{4\tilde{w}_1^2}{\tilde{w}_1^2 + w_2^2}. \tag{59}$$

Using substitutions as above, we arrive at

$$S_s(z) = \int_{\tilde{w}_a}^{\tilde{w}_b} d\tilde{w}_1 f_s(\tilde{w}_1)\exp(-2\tilde{w}_1 z_0)$$
$$f_s(\tilde{w}_1) = \frac{cp^2\left(n_1^2+n_2^2\right)\tilde{w}_1\tilde{w}_2\left(n_2^2\tilde{w}_1^2 + n_1^2\tilde{w}_2^2\right)}{3\lambda^3\left(\tilde{w}_1^2+\tilde{w}_2^2\right)\left(\tilde{w}_2^2 n_1^4 + n_2^4\tilde{w}_1^2\right)}. \tag{60}$$

Here, $\tilde{w}_2 = \sqrt{n_2^2 - n_1^2 - \lambda^2\tilde{w}_1^2}/\lambda$, $\tilde{w}_a = 0$, and $\tilde{w}_b = \sqrt{\mathrm{NA}^2 - n_1^2}/\lambda$.

The integrated supercritical axial profile is

$$F_s = \int_0^\infty dz W_s(z) = \int_{\tilde{w}_a}^{\tilde{w}_b} d\tilde{w}_1 \frac{f_s(\tilde{w}_1)}{\kappa + 2\tilde{w}_1}. \tag{61}$$

Since the factor cp^2/λ^3 in Eqs. 56 and 61 cancels out when calculating the normalized correlation function, it does not need to be further specified.

Simulations

The following Monte Carlo procedure was used to simulate TIR-FCS experiments. Numerical simulations for an ensemble of pointlike noninteracting particles were carried out in a rectangular box much larger than the detection volume for a set of discrete time instants $t_n = n\Delta t$, $n = 1\ldots N$. Every time step, an i^{th} freely diffusing particle acquired random displacements δx_i, δy_i, and δz_i, which were drawn from the Normal distribution with the variance $2D_A\Delta t$. Bound particles acquired displacements δx_k, δy_k only in the x,y plane, drawn from the Normal distribution with the variance $2D_C\Delta t$. Reflective boundary conditions were applied on all boundaries of the simulation box. Binding and unbinding dynamics were accounted for in the following way: At each time step, free particles located in the vicinity of the $z = 0$ plane within a layer of the thickness $d_{at} \approx \sqrt{2D_A\Delta t}$ were converted into bound particles with a probability $k_a B\Delta t/d_{at}$, upon which they executed two-dimensional random walks in the $z = 0$ plane until the unbinding event. The value B is the mean concentration of free binding sites. In a similar way, at each time step, bound particles were converted into freely diffusing particles with the probability $k_d\Delta t$, upon which they were placed above the $z = 0$ plane at a random z position uniformly distributed in the interval $(0, d_{at})$. The molecule detection function $\Omega(\mathbf{r})$ was taken into account to generate fluorescence intensities due to free and bound particles $F_A(t_n) = \sum_i \Omega(\mathbf{r}_i)$ and $F_C(t_n) = \sum_k \Omega(\mathbf{r}_k)$. Photon counting statistics was not included in the computed time-dependent intensity traces. Autocorrelation curves for free and bound particles as well as their cross-correlation curve were calculated from the intensity traces using a multiple tau algorithm.

Petra Schwille acknowledges support by the Max Planck society (MPI for molecular cell biology and genetics) as a Fellow.

REFERENCES

1. Thompson, N. L., T. P. Burghardt, and D. Axelrod. 1981. Measuring surface dynamics of biomolecules by total internal reflection fluorescence with photobleaching recovery or correlation spectroscopy. *Biophys. J.* 33:435–454.
2. Thompson, N. L., and D. Axelrod. 1983. Immunoglobulin surface-binding kinetics studied by total internal reflection with fluorescence correlation spectroscopy. *Biophys. J.* 43:103–114.
3. Starr, T., and N. Thompson. 2002. Local diffusion and concentration of IGG near planar membranes: measurement by total internal reflection with fluorescence correlation spectroscopy. *J. Phys. Chem. B.* 106:2365–2371.
4. Hassler, K., T. Anhut, R. Rigler, M. Gosch, and T. Lasser. 2005. High count rates with total internal reflection fluorescence correlation spectroscopy. *Biophys. J.* 88:L01–L03.
5. Ohsugi, Y., K. Saito, M. Tamura, and M. Kinjo. 2006. Lateral mobility of membrane-binding proteins in living cells measured by total internal reflection fluorescence correlation spectroscopy. *Biophys. J.* 91:3456–3464.
6. Lieto, A. M., R. C. Cush, and N. L. Thompson. 2003. Ligand-receptor kinetics measured by total internal reflection with fluorescence correlation spectroscopy. *Biophys. J.* 85:3294–3302.
7. Hansen, R., and J. Harris. 1998. Measuring reversible adsorption kinetics of small molecules at solid/liquid interfaces by total internal reflection fluorescence correlation spectroscopy. *Anal. Chem.* 70:4247–4256.
8. Sonesson, A. W., H. Blom, K. Hassler, U. M. Elofsson, T. H. Callisen, J. Widengren, and H. Brismar. 2007. Protein-surfactant interactions at hydrophobic interfaces studied with total internal reflection fluorescence correlation spectroscopy (TIR-FCS). *J. Colloid Interface Sci.* 317:449–457.
9. Lieto, A., and N. Thompson. 2004. Total internal reflection with fluorescence correlation spectroscopy: Nonfluorescent competitors. *Biophys. J.* 87:1268–1278.
10. Starr, T. E., and N. L. Thompson. 2001. Total internal reflection with fluorescence correlation spectroscopy: combined surface reaction and solution diffusion. *Biophys. J.* 80:1575–1584.
11. Thompson, N. L., and B. L. Steele. 2007. Total internal reflection with fluorescence correlation spectroscopy. *Nat. Protocols.* 2:878–890.
12. Brenner, H. 1961. The slow motion of a sphere through a viscous fluid towards a plane surface. *Chem. Eng. Sci.* 16:242–251.
13. Goldman, A., R. Cox, and H. Brenner. 1967. Slow viscous motion of a sphere parallel to a plane wall. i. motion through a quiescent fluid. *Chem. Eng. Sci.* 22:637–651.
14. Pero, J., E. Haas, and N. Thompson. 2006. Size dependence of protein diffusion very close to membrane surfaces: measurement by total internal reflection with fluorescence correlation spectroscopy. *J. Phys. Chem. B.* 110:10910–10918.
15. Zhang, B., J. Zerubia, and J.-C. Olivo-Marin. 2007. Gaussian approximations of fluorescence microscope point-spread function models. *Appl. Opt.* 46:1819–1829.
16. Aragon, S., and R. Pecora. 1976. Fluorescence correlation spectroscopy as a probe of molecular dynamics. *J. Chem. Phys.* 64:1791–1803.
17. Ries, J., T. Ruckstuhl, D. Verdes, and P. Schwille. 2008. Supercritical angle fluorescence correlation spectroscopy. *Biophys. J.* 94:221–229.
18. Enderlein, J., T. Ruckstuhl, and S. Seeger. 1999. Highly efficient optical detection of surface-generated fluorescence. *Appl. Opt.* 38:724–732.